AGU PUBLICATIONS

JGR

Journal of Geophysical Research: Space Physics

RESEARCH ARTICLE
10.1002/2015JA021569

Key Points:
- Radiation belt dynamics are a strong function of energy and L shell
- Events that fill the slot region are common at lower energies and rare at higher energies
- During enhancement events different energies are enhanced in different spatial regions

Correspondence to:
G. D. Reeves,
geoff@reevesresearch.org

Citation:
Reeves, G. D., et al. (2016), Energy-dependent dynamics of keV to MeV electrons in the inner zone, outer zone, and slot regions, *J. Geophys. Res. Space Physics*, *121*, 397–412, doi:10.1002/2015JA021569.

Received 16 JUN 2015
Accepted 22 DEC 2015
Accepted article online 28 DEC 2015
Published online 28 JAN 2016

Energy-dependent dynamics of keV to MeV electrons in the inner zone, outer zone, and slot regions

Geoffrey D. Reeves[1,2], Reiner H. W. Friedel[1,2], Brian A. Larsen[1,2], Ruth M. Skoug[1], Herbert O. Funsten[1], Seth G. Claudepierre[3], Joseph F. Fennell[3], Drew L. Turner[3], Mick H. Denton[2], Harlan E. Spence[4], J. Bernard Blake[3], and Daniel N. Baker[5]

[1]Space Science and Applications Group, Los Alamos National Laboratory, Los Alamos, New Mexico, USA, [2]The New Mexico Consortium, Los Alamos, New Mexico, USA, [3]The Aerospace Corporation, Los Angeles, California, USA, [4]Institute for the Study of Earth, Oceans, and Space and Department of Physics, University of New Hampshire, Durham, New Hampshire, USA, [5]Laboratory for Atmospheric and Space Physics, University of Colorado Boulder, Boulder, Colorado, USA

Abstract We present observations of the radiation belts from the Helium Oxygen Proton Electron and Magnetic Electron Ion Spectrometer particle detectors on the Van Allen Probes satellites that illustrate the energy dependence and L shell dependence of radiation belt enhancements and decays. We survey events in 2013 and analyze an event on 1 March in more detail. The observations show the following: (a) at all L shells, lower energy electrons are enhanced more often than higher energies; (b) events that fill the slot region are more common at lower energies; (c) enhancements of electrons in the inner zone are more common at lower energies; and (d) even when events do not fully fill the slot region, enhancements at lower energies tend to extend to lower L shells than higher energies. During enhancement events the outer zone extends to lower L shells at lower energies while being confined to higher L shells at higher energies. The inner zone shows the opposite with an outer boundary at higher L shells for lower energies. Both boundaries are nearly straight in log (energy) versus L shell space. At energies below a few 100 keV, radiation belt electron penetration through the slot region into the inner zone is commonplace, but the number and frequency of "slot filling" events decreases with increasing energy. The inner zone is enhanced only at energies that penetrate through the slot. Energy- and L shell-dependent losses (that are consistent with whistler hiss interactions) return the belts to more quiescent conditions.

1. Introduction

Almost from the time of their discovery, the radiation belts have been understood to be composed of two distinct zones of trapped energetic particles separated by a lower intensity slot region [*Van Allen*, 1959; *Van Allen and Frank*, 1959]. Those early studies referred to all trapped energetic electrons as "radiation belt electrons." *Pfitzer et al*. [1966], for example, characterized the energy and pitch angle distributions of radiation belt electrons in the inner and outer zones over energies from 50 to 4000 keV. They described the structure of the radiation belts this way: "The inner edge of the inner zone is certainly determined by the upper atmosphere of the Earth, and the outer part of the outer zone is determined by the magnetopause. The distribution of particle intensities between these places seems to show a persistent vacancy called the slot."

The inner magnetosphere contains a multitude of plasma and energetic particle populations each with different (but intertwined) dynamics. These populations include the plasmasphere, the plasma sheet, substorm injection regions, electron and ion ring current, and the proton radiation belt in addition to the inner and outer zone radiation belt populations. Contemporary studies typically treat the terms radiation belt electrons, "relativistic electrons," and "MeV electrons" synonymously which raises the question of whether tens and hundreds of keV electrons are accurately described as radiation belt electrons or whether focusing on MeV radiation belt electrons is too limited.

Figure 1 shows a schematic of radiation belt processes that illustrates some of the populations and processes that are important for radiation belt dynamics. Medium-energy (i.e., tens to hundreds keV) electrons and ions from the plasma sheet and substorm injections $E \times B$ and gradient-curvature drift sunward and eastward or westward around the Earth. If the distribution functions are unstable to the growth of waves, these electrons can become a "source population" providing the energy for waves that resonate with radiation belt electrons.

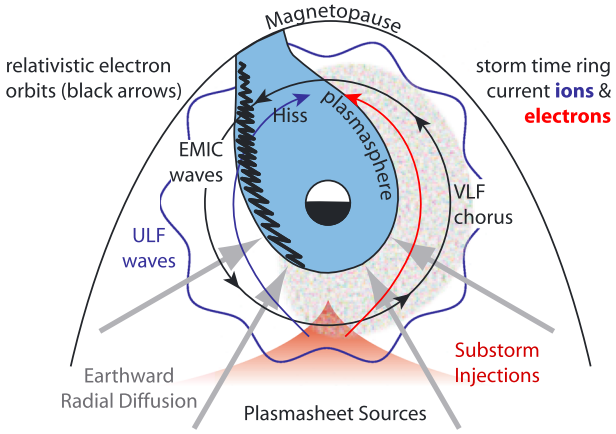

Figure 1. A schematic illustration of radiation belt structures and processes [from *Reeves et al.*, 2009].

A particularly important process is the local acceleration of MeV electrons in the outer zone consistent with acceleration by VLF whistler mode chorus waves [*Summers et al.*, 1998; *Green and Kivelson*, 2004; *Iles et al.*, 2006; *Chen et al.*, 2007; *Reeves et al.*, 2013; *Thorne et al.*, 2013; *Reeves*, 2015, and references therein]. Electrons with energies of hundreds of keV are often referred to as the "seed population" [*Obara et al.*, 2000; *Boyd et al.*, 2014; *Tu et al.*, 2014] which are accelerated to energies >1 MeV. Preexisting MeV electrons are also further accelerated to even higher energies.

The plasmasphere is a high-density region that, typically, shows a steep density gradient at the plasmapause. It fills a region where corotational $E \times B$ drift dominates over sunward $E \times B$ drift—a region that can vary greatly with the strength of the convection electric field. It is important for several reasons. First, the dramatic difference in densities inside and outside the plasmasphere affects both wave growth and radiation belt resonance conditions. Second, in steady state, the plasmapause defines a boundary that plasma sheet and substorm-injected electrons cannot penetrate. In reality though, the different time-dependent drifts of plasmasphere and plasma sheet/injection electrons can cause the populations to overlap in spatially and temporally localized regions. Third, the persistent presence of VLF whistler mode hiss inside the plasmasphere tends to scatter radiation belt electrons into the atmospheric loss cone which is thought to be the primary mechanism responsible for the formation of the radiation belt slot region [*Lyons and Thorne*, 1973]. *Li et al.* [2006] analyzed monthly averages of >2 MeV electron fluxes from SAMPEX (the Solar Anomalous and Magnetospheric Particle Explorer) and found that over many years, the inner edge of the outer radiation belt tracked the average location of the plasmapause quite closely while *Goldstein et al.* [2005] showed the same relationship on timescales of 3.5 days.

Most of the attention on the radiation belts in recent decades has focused on the dynamics of >1 MeV electrons in the outer belt. The excellent, long-term data sets from GOES and SAMPEX have been extensively studied and have focused particular attention on >2 MeV electrons. In contrast, the dynamics of tens to hundreds of keV electrons in the slot and inner zone have not been as extensively studied as the greater than MeV electrons. Measurements at these energies are extremely difficult. Protons in the proton belt with energies greater than tens of MeV cannot be shielded out, and many intended electron measurements can be shown to be dominated by penetrating protons. MeV electrons can produce high backgrounds in two ways: by direct penetration above the instrument shielding threshold and by Bremsstrahlung X-ray production in the instrument.

The Van Allen Probes satellites [*Mauk et al.*, 2012] were designed to overcome those limitations and are able to provide high temporal resolution measurements of electrons from eV to MeV. In this paper we present initial observations of keV to MeV electron dynamics in the slot and inner zone and consider potential implications for current theories of radiation belt and inner magnetospheric processes.

The paper is organized as follows. In section 1 we describe the data used in this study. In section 2 we discuss radiation belt dynamics as a function of L shell for different energies. In section 4 we describe the quiet time structure of the belts. Section 5 introduces the 1 March 2013 event. Section 6 discusses how the radiation belt fluxes are enhanced and how some energies are transported or injected earthward into and through the slot region. Section 7 discusses energy- and L shell-dependent loss rates and how the belts decay back toward a quiescent state.

2. Van Allen Probes Data

The twin Van Allen Probes Satellites have collected data continuously since October 2012. (We frequently refer to the two satellites by their prelaunch designations Radiation Belt Storm Probe (RBSP)-A and RBSP-B.) The satellites are in a near-equatorial orbit with apogee $\approx 5.8\,R_E$ and an orbital period of ≈ 9 h and a spin period

of ≈ 11 s. The Van Allen Probes satellites carry an extensive suite of particle and fields measurements. In this study we present observations from two of the three particle instruments in the RBSP-Energetic Particle, Composition, and Thermal Plasma (ECT) suite [*Spence et al*., 2013], the Helium Oxygen Proton Electron (HOPE) plasma spectrometer [*Funsten et al*., 2013], and the Magnetic Electron Ion Spectrometer (MagEIS) [*Blake et al*., 2013].

HOPE measures electrons and ions (with composition) from 1 eV (or spacecraft potential) to 50 keV in 5 look directions and 72 energy steps with energy resolution $\Delta E/E \approx 15\%$. It uses a spherical electrostatic analyzer followed by time of flight (TOF) chambers and channel electron multipliers. The instrument was designed with detectors that are quite insensitive to penetrating backgrounds. In addition, careful accounting start, stop, and TOF signals actively reject backgrounds from radiation that does penetrate the shielding [*Funsten et al*., 2013].

MagEIS measures electrons from 20 keV to 4.8 MeV using four magnetic spectrometers covering three overlapping energy ranges and ions from 55 keV to ~20 MeV using a range telescope. The two MagEIS medium units provide different fields of view and pitch angle coverage. The magnetic spectrometers focus electrons within a selected energy pass band upon a focal plane of several silicon detectors where pulse-height analysis is used to determine if the energy of the incident electron is equivalent to the electron momentum selected by the magnet. Thus, each event is a two-parameter analysis, an approach leading to a greatly reduced background. Additionally, in "histogram mode," the solid-state detectors measure the full spectrum both inside and outside the energy passband selected by the spectrometer. Since the energy selection is strictly controlled by the magnetic spectrometer, signals outside the primary detector passband are all background [*Blake et al*., 2013]. Ground-based processing software can then determine the signal-to-noise ratio in each energy bin and actively subtract any backgrounds that contribute to the signal within the primary passband [*Claudepierre et al*., 2015; *Fennell et al*., 2015].

In addition to their design features, both instruments are heavily shielded making the HOPE and MagEIS measurements the best to date for unambiguously measuring the dynamics of keV to MeV electrons in the slot and inner zone. (The third ECT instrument, the relativistic electron proton spectrometer [*Baker et al*., 2012], provides similar measurements at higher energies than are used in the current study.) In this analysis, for both instruments, we use release three of the spin-averaged, ≈11 s data available at http://www.rbsp-ect.lanl.gov.

3. Energy-Dependent Dynamics

Figure 2 shows electron flux as a function of L shell and time for the year 2013. Figures 2a–2e show five energies, 1553 keV, 459 keV, 234 keV, 110 keV, and 46 keV, respectively. To ease comparison, all fluxes are plotted on scales covering 3 orders of magnitude but with different absolute ranges. Figures 2f–2h show solar wind speed, the interplanetary magnetic field (IMF) B_z, and the *Dst* index from OMNIWeb (http://omniweb.gsfc.nasa.gov).

The 1553 keV electron panel (Figure 2a) shows relativistic electron dynamics that are familiar from observations by missions such as CRRES [*Vampola et al*., 1992], Polar [*Blake et al*., 1995], and SAMPEX [*Baker et al*., 1993]. The dynamics of the outer zone are dominated by episodic events that enhance or deplete fluxes in response to geomagnetic activity: storms, southward IMF, and high solar wind speed [*Reeves et al*., 2003]. These observations are some of the first, however, that are essentially free of background contamination from bremsstrahlung X-rays and penetrating particles [*Claudepierre et al*., 2015]. As *Fennell et al*. [2015] have shown, the main feature that differs from the expected behavior is that there are essentially no >1 MeV electrons in the inner zone at levels above background. We know that the inner zone occasionally gets replenished during high geomagnetic activity when MeV electrons penetrate through the slot region, deep into the inner magnetosphere as was observed in the Halloween 2003 event [*Baker et al*., 2004]. However, during 2013 no such events were observed and the inner edge of the outer zone MeV electrons never penetrated deeper than $L \approx 3$ [*Baker et al*., 2014].

At 459 keV (Figure 2b) the radiation belts have the expected two-zone structure with a very dynamic outer zone, a fairly stable inner zone, and a slot region. The inner zone has somewhat lower flux levels than the outer zone. Figures 2c–2e show electrons with energies of 234, 110, and 46 keV, i.e., energies that are usually associated with "seed" or "source" populations. Yet even at these relatively low energies radiation belt-like features still exist. Specifically, there is a highly dynamic outer zone region with episodic enhancements of electron fluxes, a much less dynamic inner zone that is replenished during some of the outer zone enhancement events, and a slot-like region where quiet time fluxes are orders of magnitude lower than in the inner or

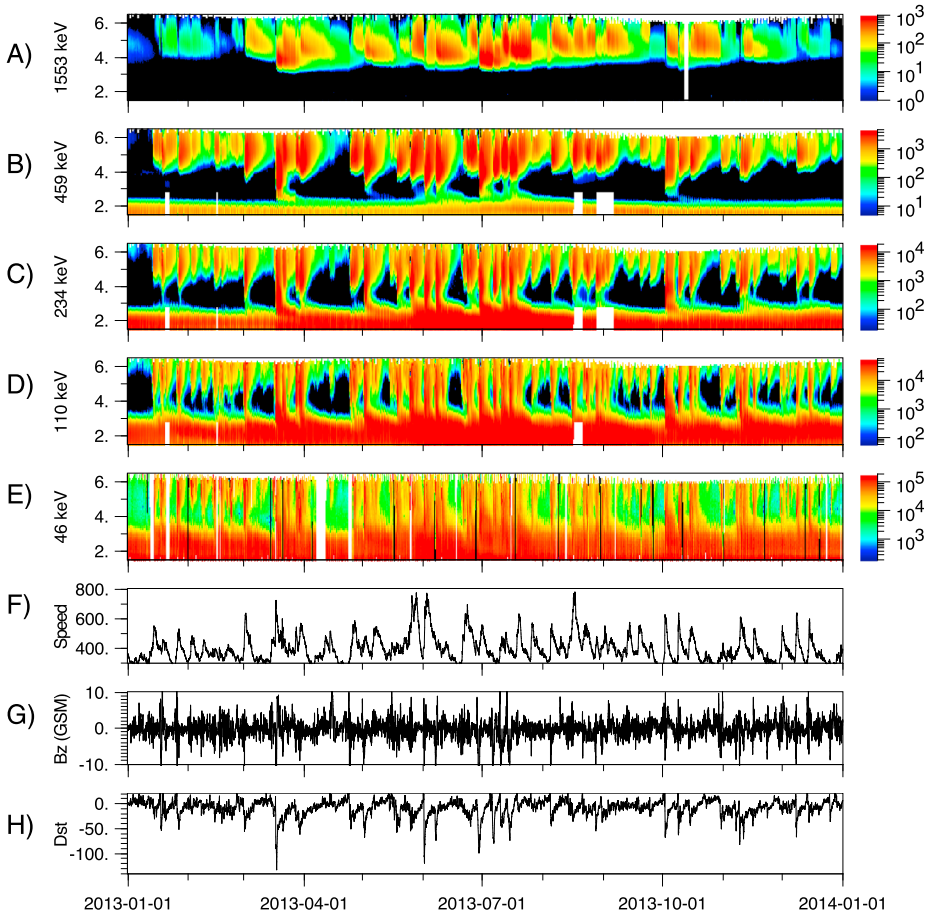

Figure 2. A multienergy view of flux as a function of L shell and time from the Van Allen Probes mission for 2013. (a–d) Background-corrected MagEIS electron fluxes, (e) electron fluxes from HOPE, and (f–h) geomagnetic indices: solar wind speed, IMF B_z, and *Dst*. Dramatic differences in radiation belt electron behavior are seen at different energies and from event to event.

outer zones. This suggests that electrons with energies as low as tens of keV can indeed be considered radiation belt electrons and are likely affected by at least some of the same processes that control radiation belt dynamics at MeV energies.

In Figure 3 we compare the number of flux enhancement events as a function of energy and L shell for the first half of 2013. As also seen in Figure 2, at any given L shell there are more events at lower energies than there are at higher energies. For example, at L −3.5 there were 22 events observed at 46 keV and only 4 events at 1.5 MeV. We note that the events at higher energies are always a subset of the lower energy events; i.e., there were no events identified at higher energies that were not also present at lower energies. Figure 3 also shows that at any given energy, there are fewer events that penetrate to low L shells. At 459 keV there were 15 events observed at $L = 5.5$. Of those 13 (87%) penetrated to $L = 4.5$ and 9 (60%) penetrated to 3.5 but only 4 (3%) penetrated to 2.5.

To further investigate the energy dependence of penetration into and through the slot region, we return to Figure 2. At 1.5 MeV none of the events in 2013 extended below about $L = 3$, and no enhancement events were observed at $L = 2.5$. At 459 keV at least seven events in 2013 show flux enhancements that inject particles that penetrate through the slot region and at 234 keV there were at least 24.

Summarizing these observations:

1. Outer Zone Enhancements: At lower energies there tend to be more electron enhancements than at higher energies. Or, said another way, a given event is more likely to produce an enhancement of lower energy

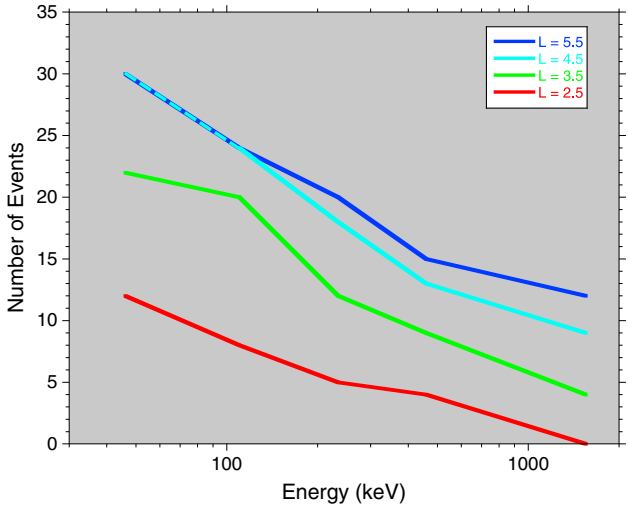

Figure 3. The number of radiation belt enhancement events in the first 6 months of 2013 as a function of energy at L shells ranging from 2.5 to 5.5. We identify enhancement events visually when line plots of fluxes at fixed L shell show rapid increase, slower decay, and exceed a fixed flux threshold. At all L shells there are more events at lower energy than at higher energy. At a given energy fewer events penetrate to lower L shells than are observed at higher L shells. Most events that penetrate to $L = 5.5$ also penetrate to $L = 4.5$, but few of them penetrate to $L = 2.5$.

electrons than it is to produce an enhancement at the higher energies. Notice, for example, the quiet period in September when 234 keV electrons show three clear enhancements, but 1553 keV electrons show only one.

2. Slot: In any given enhancement event lower energy electrons are more likely to fill the slot region and penetrate into the inner zone. Similarly, even when they do not fill the slot, lower energy electrons penetrate to lower L shells than higher-energy electrons.
3. Inner Zone: Enhancements of electrons in the inner zone are more common at lower energies, but interestingly, not every slot filling event produces long-lasting enhancements of inner zone fluxes. In addition, even in quiet times, the inner zone extends to higher L shells for lower energies, and consequently, the slot region is also found at higher L shells.

Finally, we note that essentially, every feature of the radiation belts is energy dependent and exhibit a striking coherence across a broad spectrum of energies. We see energy dependence during flux enhancement events and in the relatively quiet times between enhancement events. We will examine both in more detail in the next sections.

4. Quiet Time Structure

In this section we explore the energy-dependent structure of the radiation belts during relatively quiet times. This provides a baseline against which to compare the episodic enhancement and transport of outer belt electrons into and through the slot region. The features we will discuss are the typical features observed between enhancement events, but it is important to note that enhancement events come too frequently to call the quiescent conditions "equilibrium" states.

Figure 4 provides a view on the energy-dependent structure of the radiation belts in a different format than is commonly used. Here we plot electron flux as a function of L shell over a very broad range of energies spanning 1 keV to 4 MeV. This "broad-spectrum" format provides a complementary view to the more traditional plots of L shell and time at several fixed energies (e.g., Figure 2).

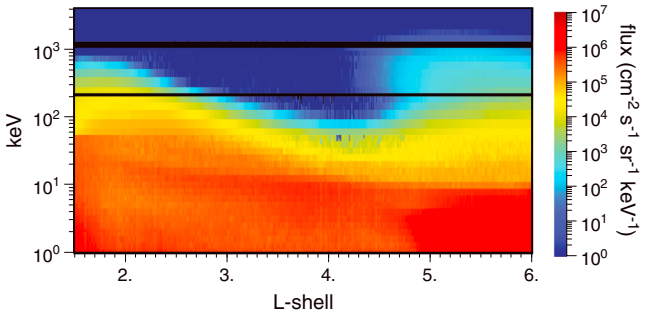

Figure 4. HOPE electron fluxes from 1 to 50 keV (<1 keV HOPE data are not considered in this study) and background-corrected MagEIS data from 50 keV to 4 MeV plotted as a function of energy and L shell. This shows on pass through the radiation belts during quiet times: the inbound leg of RBSP-A orbit 485 (11:14 to 15:43 UT on 27 February).

Figure 4 plots HOPE data from 1 to 50 keV (<1 keV HOPE data are not considered in this study) and background-corrected MagEIS data from 50 keV to 4 MeV. The gaps in MagEIS coverage are energy channels where the current background correction algorithm has not been fully validated.

Extending the observations down to 1 keV highlights the fact that the inner zone is actually the dominant structure

of the radiation belts during quiet times. One of the clearest features of the inner zone population is its energy-dependent outer edge. As was shown in Figure 2 the outer edge of the inner belt is observed at low L shells for high energies and at higher L shells for lower energies. At ~ 800 keV the inner zone extends out to only $L \approx 2$ while at ~50 keV it extends to $L \approx 4$. This format also shows more clearly that the L dependence is continuous over a wide range of energies; from ~800 keV down to as low as ~10 keV.

The outer zone electrons in this period are also clearly visible but since this was chosen as a relatively quiet time, their fluxes are relatively low. There is an interesting, and somewhat unexpected, energy dependence to the inner edge of the outer zone. At $L \approx 4.5$ (in this case) there is a minimum in flux as a function of energy which appears in this format as a "bite out" in the outer zone at energies of few 100 keV. The result is an inner boundary to the outer belt that could be described as "S shaped."

The combined energy-dependent structures of the inner zone and outer zone create an energy-dependent slot region. At energies where there is a clear minimum in the slot (≈10 keV to ≈ 1 MeV for this time) the slot is wider and deeper at high energies and is narrower and shallower at low energies. Where fluxes are substantially above background, the location of the slot minimum is found at higher L shells for lower energies.

Returning to Figure 2, it is apparent that the detailed energy-dependent state of the radiation belts is a function of the preceding enhancement event and the amount of time since that event. In the following sections we show that the features seen in Figure 4 are produced by a combination of acceleration, transport, and loss processes.

5. The 1 March 2013 Enhancement Event

In this section we discuss the energy- and time-dependent structure of the radiation belts spanning an enhancement event that started on 1 March 2013. Figure 5 shows the solar wind speed, IMF B_z, *AE* index, *Dst* index, and RBSP-A orbit from 21 February to 13 March 2013. The event started late on 28 February with a modest interval of southward IMF and increasing solar wind speed. The next-day solar wind speeds peaked at nearly 650 km/s and *Dst* dipped below -50 nT.

Figure 6 shows how the energy-dependent structures in the radiation belts develop and evolve during the 1 March enhancement event. Each plot shows data from the inbound half of the orbit (i.e., apogee to perigee) for RBSP-A. Each orbit is separated in time by ~9 h, and each inbound pass takes ~4.5 h.

Figure 6 (left column) shows the enhancement of fluxes and transport into and through the slot region. The enhancement and transport occur over five orbits that span the ~2 day interval from 28 February at 09:41 UT before the solar wind driving intensified through the main phase of the storm, ending 2 March at 02:03 UT.

Orbits 487 and 488 show the quiet time structure that was discussed in the previous section. This quiescent state had persisted for many previous orbits. The first signs of the enhancement event in Figure 6 appear on orbit 489 as substorm-injected electrons began to penetrate to lower L shells. Intense substorm injection activity continued through orbit 490 but diminished somewhat on orbit 491. (Substorm injection activity is presented in Figure 8 and will be discussed in more detail later.)

By orbit 490 the flux of outer zone electrons at all energies below 1 MeV had been enhanced, and the inner boundary was shifted to lower L shells. Substantial fluxes of 200 keV electrons were observed below $L \approx 3.5$, while on the previous orbit they only appeared above $L \approx 4.0$. At energies close to 1 MeV the change is subtle, but there is still an inward motion of the boundary of $\Delta L \lesssim 0.1$. We note, however, that on orbit 490, RBSP-A had not yet seen any enhancement of >1 MeV electrons.

On orbits 491 and 492, as geosynchronous substorm injection activity continued and *Dst* remained low, the trends in the radiation belt enhancement continued. By then fluxes of >1 MeV electrons in the outer zone were enhanced above preevent levels, while fluxes of electrons with energies less than 1 MeV continued to penetrate to lower L shells. For this event, substantial filling of the slot region was observed at all energies up to ~300 keV but not much above that energy.

Orbit 491 ended at 02:05 on 2 March by which time the enhanced structure of the radiation belts could be called "fully developed." The characteristics of the fully developed 1 March enhancement event include (a) enhanced fluxes in the outer belt at energies up to >3 MeV and (b) filling of the slot region at and enhanced

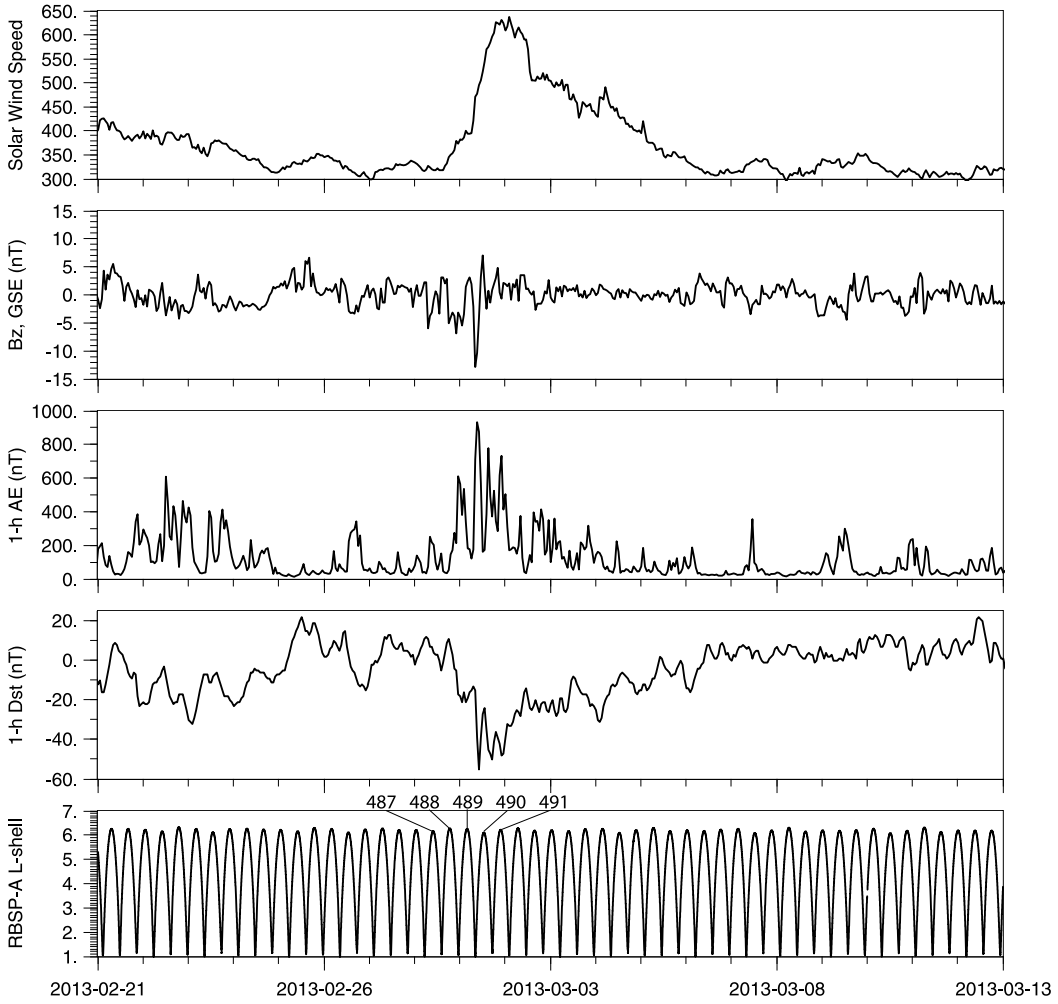

Figure 5. Solar wind speed, IMF B_z, *AE*, *Dst*, and the orbital L shell for RBSP-A are shown for the 1 March 2013 radiation belt enhancement event. Orbits 487 through 491 are noted for reference.

fluxes of electrons in the inner zone at energies up to ~300 keV, but (c) no filling of the slot or change in the fluxes of inner zone electrons above ~300 keV.

We also note, in particular, a rather unexpected feature of the outer zone electrons. The inner edge of the active-time outer belt is highly energy dependent and can be fit quite well with a straight line in log(energy) versus L shell.

To quantify the energy dependence of the boundary, we used the steepest slope on the radial gradient to define the energy dependence more quantitatively. For the 336 keV channel the steepest gradient is located between $3 < L < 4$ with a midpoint of $L \approx 3.5$. In the 737 keV channel the steep gradient lies between $3.5 < L < 4.2$ with a midpoint at $L \approx 3.8$ and a midpoint of the 2.2 MeV channel at $L \approx 4.5$. As is also suggested by the color contours in Figure 6, those points define a straight line in log(energy) versus L, specifically $L_{min} = 0.3 + 1.2 \log(E)$ with E in keV.

Figure 6 (right column) shows the evolution of the radiation belts over the next ~4 days. The decay of electron fluxes in the slot region begins almost immediately and quickly returns the belts to a quiescent state quite similar to the state the existed prior to the enhancement event.

6. Radiation Belt Enhancement and Transport Through the Slot

The intent of this paper is primarily to document, observationally, the energy- and L shell-dependent states of the radiation belts and the transitions from quiescent to enhanced and back to quiescent. It is, however,

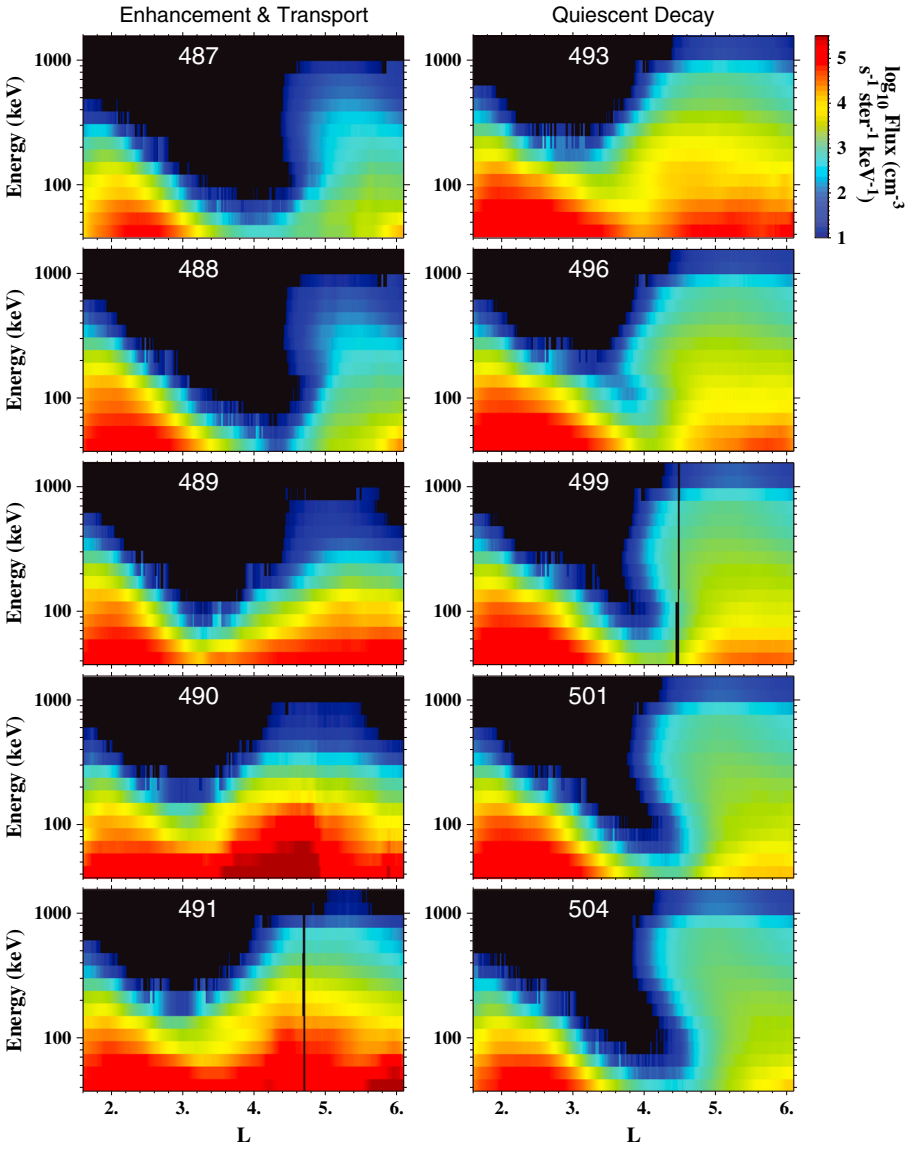

Figure 6. Color-coded MagEIS background-corrected electron fluxes plotted as a function of energy and L shell. Only inbound passes from RBSP-A are plotted. (left column) (Orbits 487–491) the enhancement and transport of electrons over ~2 days. (right column) Selected orbits over the ~4 days following the event when electron fluxes were decaying.

natural to ask why the enhancement and transport of electrons to low *L*, into the slot, and/or into the inner zone are so energy dependent, why they vary from event to event, and what physical processes are responsible? Answering those questions will, no doubt, take further observational, theoretical, and modeling studies. But, here we explore, briefly, the possible roles that storm time convection and substorm-like injections might play.

Figure 7 shows four electron energies as line plots that highlight the flux enhancements and earthward transport. The lines are color coded by orbit running from orbit 487 in blue to orbit 491 in red. The outbound and inbound legs are at different local times, so both spatial and temporal differences can be seen—particularly at low energies.

For all four energies there is a distinct slot at the beginning of the interval on orbit 487 (blue lines). By orbit 491 (red lines, 36 h later) the slot is completely filled at energies up to at least 146 keV and large increases of fluxes in the slot are observed up to at least 336 keV. The filling is remarkably rapid. Each orbit is only 9 h, and the entire interval plotted is only 45 h (28 February, 5:11 UT to 2 March, 2:00 UT).

Figures 7 (first panel) and 7 (second panel) show quite dynamic variations from pass-to-pass down to at least $L < 3$. These variations are highly suggestive of substorm injections. *Turner et al.* [2015] presented a case study

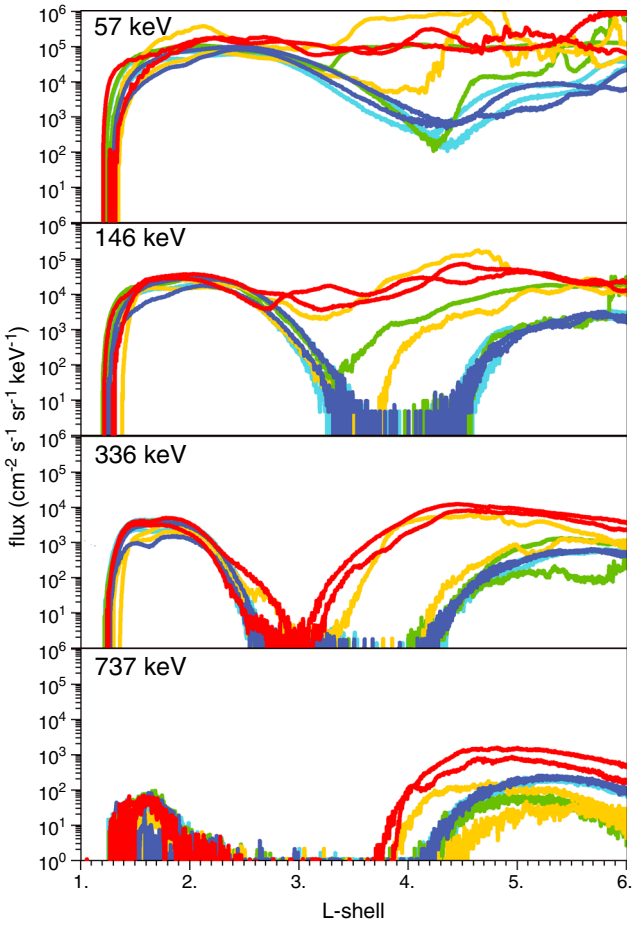

Figure 7. Flux as a function of L-shell for four different energies. Both outbound and inbound passes are plotted and are color-coded by orbit. Orbit 487, starting Feb. 28 at 5:11 UT (blue); orbit 488 (cyan); orbit 489 (green); orbit 490 (orange); and orbit 491, ending March 2 at 02:00 UT (red). Each orbit takes ~9 hours. The inbound and outbound legs sample different local times. Substorm injections, filling of the slot region, and earthward penetration of the outer zone are all apparent.

that clearly linked an injection seen at $L \approx 2.5$ to substorm activity seen at geosynchronous orbit and beyond. Figure 8 presents substorm injection activity on 1 March 2015 from six Los Alamos National Laboratory (LANL)-GEO satellites along with data from Van Allen Probes (A and B). The first injection occurred at ~23:00 on 28 February. It does not appear in Figure 6 because RBSP-A was at perigee at the time. The first injection seen by RBSP-A occurred around 01:30 on 1 March. Injection frequency increased again starting around 08:00 UT and continued for the remainder of the day and into 2 March when *Dst* began to recover (Figure 5).

Previous studies have shown that the "injection front" (the earthward edge of the dispersionless injection region) moves earthward inside geosynchronous orbit with a speed of tens of km/s [*Reeves et al.*, 1996; *Malaspina et al.*, 2014] at least to the vicinity of $L \approx 4.5$ [*Friedel et al.*, 1996], but it is hard to imagine that the inductive fields that produce dispersionless substorm injections extend down to $L \approx 2.5$. *Turner et al.* [2015] attributed the deep injection to a two-step process involving dispersionless substorm injections and further transport by a fast magnetosonic wave at Pi2 frequencies.

A third mechanism that may play an important role is enhanced cross-tail electric fields driven by dayside reconnection. Enhanced storm time convection increases the sunward directed convective flow and pushes the (energy-dependent) Alfvén boundaries earthward on the nightside. *Thaller et al.* [2015] analyzed the event on 1 June 2013 and found ~1–2 mV/m electric fields down to L shells as low as ~2.3. There is no question that this strong convective transport can, in principal, open up drift paths that bring ions and electrons deep into the inner magnetosphere.

The differences between electron and ion dynamics, however, suggest that enhanced storm time convection alone cannot produce the observed slot-filling effects. This can be seen by comparing the ion fluxes plotted in Figure 9 with the electrons plotted in Figures 2 and 6. At 20 keV, electrons, protons, oxygen, and helium can all be injected to very low *L*. But, in 2013, 140 keV protons are never injected below $L \approx 3$ whereas electrons of the same energy routinely are. For the 1 March event, 140 keV ions fluxes were only enhanced down to $L \approx 4$ whereas 146 keV electrons fluxes were enhanced down to $L \approx 2.5$. The competing effects of corotation and gradient-curvature drifts should, if anything, bring ions deeper into the magnetosphere than electrons.

We also considered if charge exchange losses could mask possible ion injection signatures at low *L*. If charge exchange were faster than transport, then ions might be lost before they could be injected whereas electrons would not be. This does not seem to be the explanation though. Since 20 keV protons are injected below $L \approx 3$, earthward transport of 20 keV protons must be faster than losses due to charge exchange. Charge exchange is slower even slower for 140 keV protons than it is for 20 keV protons, so if earthward transport is faster than losses at 20 keV, then earthward transport is much faster than losses at 140 keV.

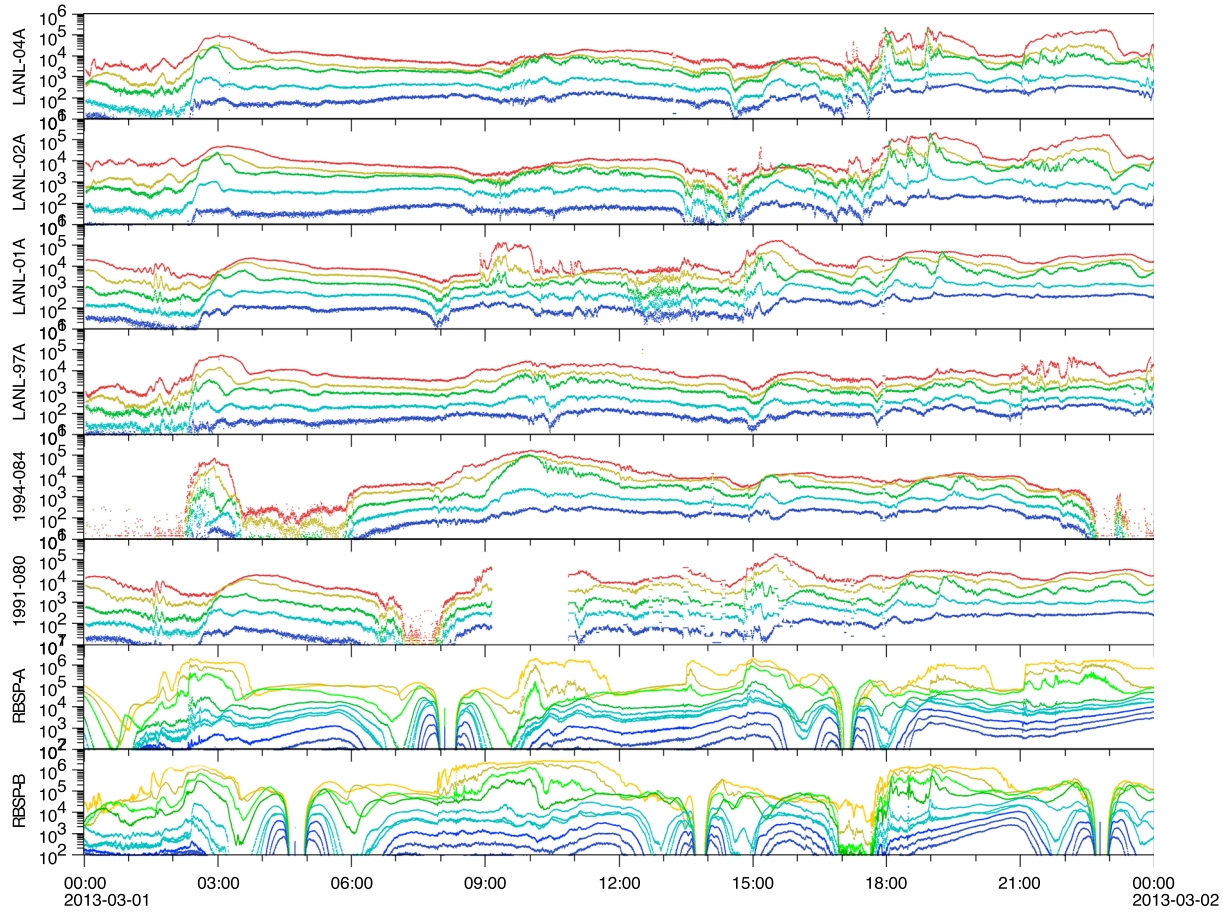

Figure 8. Substorm injection activity on 1 March 2013 measured at geosynchronous orbit and by the two Van Allen Probes satellites in elliptical orbits. The LANL-GEO Synchronous Orbit Particle Analyzers (SOPA) electron data spans ~50 to ~500 keV and RBSP data spans ~40 to ~600 keV.

It is likely that 140 keV protons do not penetrate as deeply as 20 keV protons because gradient-curvature drifts become dominant. However, gradient-curvature drifts also affect electrons, so the difference between ion and electron behavior must be attributed to some other transport or acceleration processes that act on electrons but not ions.

Local acceleration by wave-particle interactions is one such process. The observations of the 1 March 2013 event does show characteristics that may be consistent with local acceleration—particularly at energies above those that penetrate the slot. However, the energy-dependent earthward boundary of the outer zone is difficult to reconcile with local acceleration alone. Chorus should accelerate electrons over a wide range of energies wherever chorus is present. While it may be possible for chorus acceleration to produce an inner edge of the outer belt that is linear in log(energy) versus L shell, it is not readily apparent how that would happen.

Since no one mechanism seems able to account for the observations, it is probable that several different mechanisms are acting together. Direct substorm injections, enhanced earthward convection, local acceleration and some additional earthward transport process such as magnetosonic wave resonance may all act in combination to produce the energy-dependent earthward transport of radiation belt electrons, filling of the slot region, and injection into the inner zone.

7. Recovery From Enhanced to Quiescent States (Losses)

We now consider the recovery of the 1 March 2013 event from enhanced to quiescent states and discuss the role of electron losses, pitch angle scattering, and plasmaspheric hiss. Figure 6 shows the evolution of the slot region over the ~4 days immediately following the enhancement. The decay of electron fluxes in the region

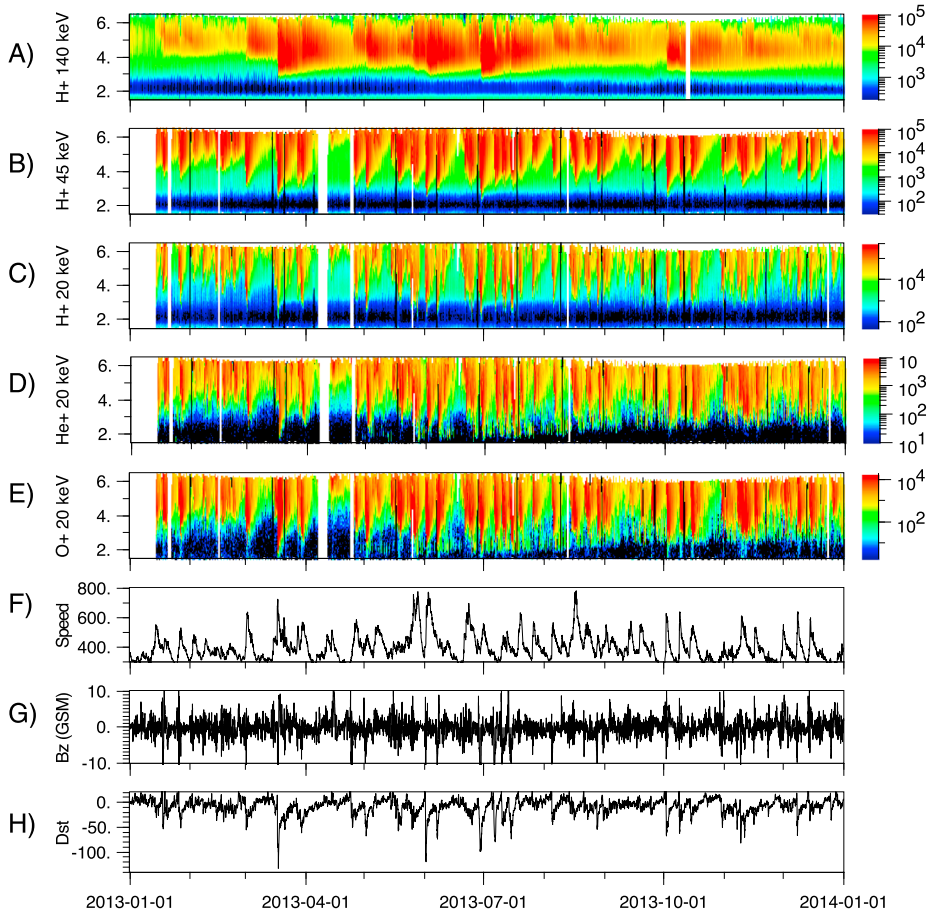

Figure 9. Ion fluxes as a function of L shell and time along with solar wind speed, B_z, and *Dst* plotted in the same format in Figure 2. (a) 140 keV MagEIS ion measurements. (b) 45 keV HOPE protons. (c–e) 20 keV protons, helium ions, and oxygen ions. Ions with 20 and 45 keV energies penetrate more deeply and decay more quickly than at 140 keV. Comparison with Figures 2 and 7 shows that ~140 keV electrons fill the slot quite frequently in 2013 while 140 keV ions were not injected below $L \approx 3$.

$L \approx 2.5$–4 begins almost immediately. It is apparent that the rate of decay depends both on L shell and on energy. For example, at $L = 4.5$ the fluxes of 70 keV electrons decrease more quickly than at 700 keV. Specifically, Figure 10 shows the flux as a function of time for four energies and two L shells. At $L = 5$, in the heart of the outer belt, lifetimes become longer and longer with increasing energy. In contrast, at $L = 4$ the lifetimes at 146 and 336 keV are shorter than they are at higher (737 keV) or at lower (57 keV) energies. It is these energy- and L shell-dependent loss rates that create the bite-out and S-shaped outer belt boundary that was discussed previously.

Similar energy and L dependencies to the loss rates create the inner zone. For example, at $L = 3$ the fluxes of 200 keV electrons decrease more quickly than the fluxes of 50 keV electrons leaving a sharp boundary to the inner zone that can be described approximately by $L_{max} = 7–2 \log(E)$ with E in keV.

The different loss rates as a function of energy and L shell discussed here are based only on observations and do not depend on any particular physical mechanism. We note, however, that losses at these energies and L shells have often been attributed to pitch angle scattering from whistler mode hiss [*Lyons et al.*, 1972; *Lyons and Thorne*, 1973; *Santolík et al.*, 2001; *Meredith et al.*, 2006, 2007; *Summers et al.*, 2007; *Ripoll et al.*, 2014, 2015; *Li et al.*, 2015].

Meredith et al. [2007] calculated electron lifetimes for plasmaspheric hiss as a function of energy and L and found that at $L = 4$ the minimum lifetime occurred for ~200 keV consistent with our results. They also found that at lower L shells, the lifetimes for a given energy got progressively longer which likely explains the energy dependence of the inner zone population. More recently, J.-F. Ripoll et al. (Highly resolved

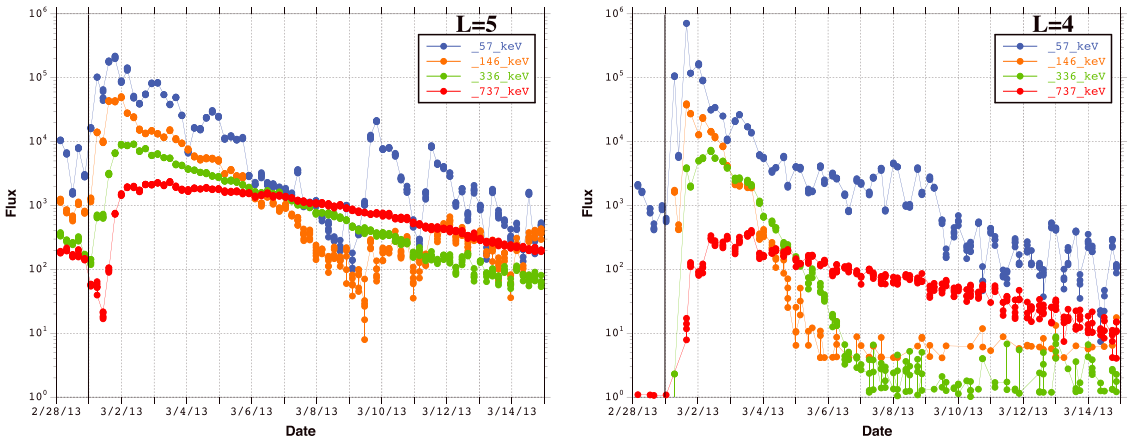

Figure 10. Flux as a function of time for four different electron energies (57–737 keV) at $L = 5$ and $L = 4$. All curves show the exponential decay expected for losses from pitch angle scattering by whistler mode waves. At $L = 5$ lifetimes are shorter for lower energies and longer for higher energies, but at $L = 4$ the lifetime of 146 and 336 keV electrons are shorter than at higher (737 keV) or lower (57 keV) energies. The minimum lifetimes at a few 100 keV at $L = 4$ are consistent with expectations from hiss and are what produce the bite out of fluxes in that range of energy-L space as seen in, e.g., Figure 4.

effects of whistler-mode hiss waves in March 2013, Journal of Geophysical Research, manuscript in preparation, 2015) used Van Allen Probes plasma and wave observations for the same 1 March 2013 event to calculate electron lifetimes as a function of energy and L shell and found good agreement with the observed lifetimes presented here.

8. Conclusions

We have presented an analysis of the dynamics of the radiation belts from the Van Allen Probes mission. Newly available data that have had penetrating background removed enables studies in the slot and inner zone that were previously ambiguous or difficult to interpret. The high-energy-resolution measurements from HOPE and MagEIS show that radiation belt dynamics are coherent across a broad range of energies down as low as a few tens of keV. Even tens and hundreds of keV electrons show a spatial structure with an inner zone, slot, and outer zone commonly thought to be typical of the radiation belts, but above 1 MeV the "typical" inner zone is absent throughout 2013.

We investigated the energy-dependent dynamics of radiation belt enhancements at multiple energies (Figures 2 and 3). We found that (1) at any given L shell there are more enhancement events at lower energy than there are at higher energies; (2) enhancement events therefore appear to have an upper energy limit that varies from event to event; (3) at any given energy the number of events observed decreases with L but some events penetrate more deeply than others; (4) therefore, in any given event lower energy electrons are more likely to fill the slot region and penetrate into the inner zone; (5) electrons that do penetrate through the slot have an upper energy "threshold," but the maximum energy varies from event to event; and (6) enhancements in the inner zone are also more common at lower energies, but not every slot-filling event produces long-lasting enhancements of inner zone fluxes.

Broad-spectrum plots of flux as a function of energy and L shell show additional energy-dependent features that are not as readily apparent in multienergy plots of flux as a function of L shell and time. Figure 11 summarizes our results for quiet and active conditions. During quiet conditions the inner zone has an outer boundary that is nearly linear in log(energy) versus L and the outer zone has an inner boundary that is S shaped with a bite out of fluxes at a few 100 keV. During active conditions electrons are injected into (and/or accelerated within) the slot region and fill the slot up to some maximum energy threshold. Above that threshold lower energies penetrate still penetrate to lower forming an energy-dependent inner boundary to the active outer belt that is also often remarkably linear in log(energy) versus L thus forming a pair of boundaries shaped something like a "V." Subsequent energy-dependent losses remove the electrons that were injected into the slot and reform a linear inner zone boundary and an S-shaped outer zone boundary.

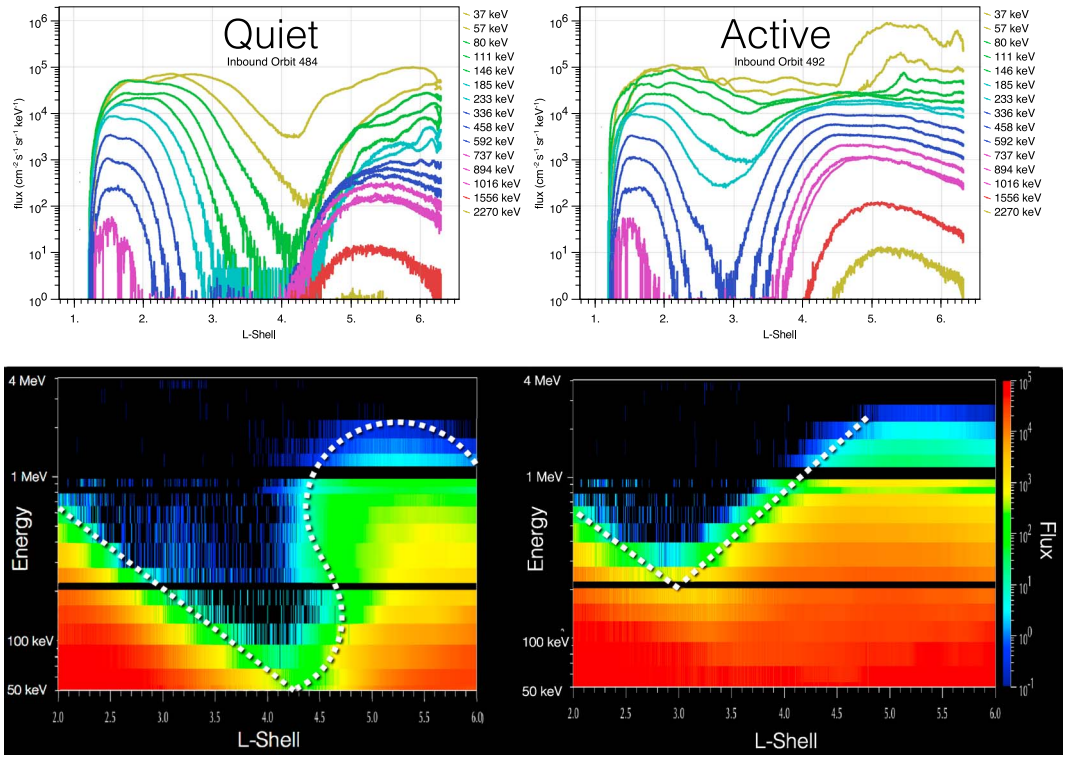

Figure 11. Flux as a function of energy and L shell for quiet (inbound orbit 484) and active (inbound orbit 492) conditions. Under quiet conditions the inner zone has a triangular shape with an outer boundary that is nearly linear in log(energy) versus *L*. During 2013 the inner zone population only extended up to energies $\lesssim$ 1 MeV. The outer zone shows a "wave-like" structure with and energy-dependent inner boundary. The energy-*L* structure implies that over some range, higher energy electrons have higher fluxes than lower energy electrons as seen in the line plot. In quiet times there is a flux minimum in the slot region down to energies of tens of keV. In active conditions outer zone electron fluxes are enhanced producing an inner boundary that is closer to the Earth at lower energies than at higher energies. Fluxes in the slot region are enhanced over a broad range of energies, and up to some threshold energy, the slot is completely filled in. At energies above that threshold the inner zone fluxes are replenished, while above that threshold the inner zone fluxes are unaffected.

The general morphology during active and quiet time conditions shows remarkable similarities among events. Figure 12 presents this broad-spectrum view for six additional events from March to June 2013 as marked in Figure 12a. In Figures 12b–12m each row shows a different storm. Figures 12b, 12d, 12f, 12h, 12j, and 12l show the quiescent state before the storm, and Figures 12c, 12e, 12g, 12i, 12k, and 12m show the active conditions near the peak of the storm. While there are important and interesting differences, all six events show striking similarities to the 1 March event. In particular, in active conditions (Figures 12c, 12e, 12g, 12i, 12k, and 12m) all events show an inner boundary for the outer belt that is strongly energy dependent. In order to better see the penetration and filling of the slot region, we have drawn a straight line approximating the energy dependence of the enhanced outer zone fluxes and reproduced same lines on the plots of the quiescent states before the events. Interestingly, for the 24 April and 1 May events, the preexisting population of high-energy electrons at low L shells (i.e., to the left of the dashed line) is relatively unaffected by the enhancement event.

The quiescent conditions before these events show more variation than the active conditions do. As can be seen from Figure 12a, this is at least in part a function of the intensity of the previous enhancement and the length of time between events when the electron fluxes are decaying. For example, prior to the 17 March and 24 April events the slot was much broader in *L* and extended to lower energies than the 1 and 7 June events. At times the upper and lower portions of the S-shaped boundary are highly asymmetric but retain the characteristic bite out that defines the lower portion of the S. It is also interesting to consider sequential events. Figure 12j shows the quiet state of the radiation belts before the event on 1 June, but it is also the quiet state resulting from the decay of the event on 25 May (Figure 12i). The same applies to Figures 12k–12m.

Despite important quantitative differences, the broad-spectrum plots in Figures 11 and 12 all show qualitatively similar energy dependencies and behaviors both in active conditions when fluxes are accelerated and injected and in the quiet conditions when fluxes are decaying. The strong coherence

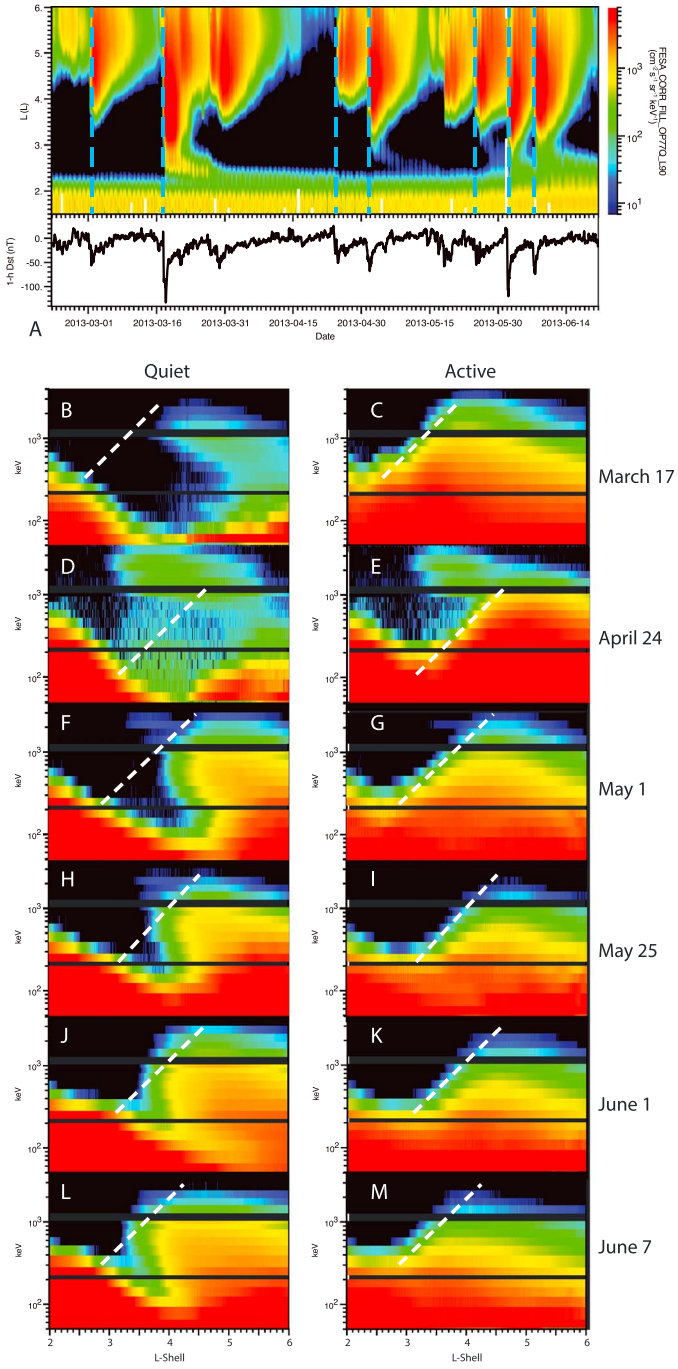

Figure 12. Energy-dependent dynamics for five additional events in 2013. (a) 459 keV flux as a function of *L* and time along with the *Dst* index. Event times are marked with dashed lines. (b–m) Flux as a function of energy and L shell for individual orbits prior to an enhancement event (Figures 12b , 12d, 12f, 12h, 12j, and 12l) and during the active part of the event (Figures 12c, 12e, 12g, 12i, 12k, and 12m). Figures 12b–12m use arbitrary color scales that keep the dynamic range approximately the same for each event. The orbits plotted are Figure 12b: 529; Figure 12c: 535; Figure 12d: 633; Figure 12e: 637; Figure 12f: 651; Figure 12g: 655; Figure 12h: 713; Figure 12i: 718; Figure 12j: 732; Figure 12k: 737; Figure 12l: 748; and Figure 12m: 753.

across a broad range of energies and the qualitative similarities among events need to be better understood. They must also provide clues about the underlying processes that may be common to all radiation belt enhancement events but that are obscured by the strong differences among events when viewed at fixed energies or spatial locations.

Acknowledgments
This work was supported by RBSP-Energetic Particle, Composition, and Thermal Plasma funding under NASA's prime contract NAS5-01072. The authors acknowledge the International Space Sciences Institute (ISSI) and the participants in a 2014 ISSI workshop, particularly Matina Gkioulidou, Jean-Francois Ripoll, and Ondrej Santolik. All Van Allen Probes (RBSP) observations used in this study, along with display and analysis software, are publicly available at the Web site http://www.RBSP-ect.lanl.gov/.

References

Baker, D. N., G. M. Mason, O. Figueroa, G. Colon, J. G. Watzin, and R. M. Aleman (1993), An overview of the solar, anomalous, and magnetospheric particle explorer (SAMPEX) mission, *IEEE Trans. Geosci. Remote Sens.*, *31*, 531–541, doi:10.1109/36.225519.

Baker, D. N., S. G. Kanekal, X. Li, S. P. Monk, J. Goldstein, and J. L. Burch (2004), An extreme distortion of the Van Allen belt arising from the Halloween solar storm in 2003, *Nature*, *432*(7019), 878–881.

Baker, D. N., et al. (2012), The relativistic electron-proton telescope (REPT) instrument on board the Radiation Belt Storm Probes (RBSP) spacecraft: Characterization of Earth's radiation belt high-energy particle populations, *Space Sci. Rev.*, doi:10.1007/s11214-012-9950-9.

Baker, D. N., et al. (2014), An impenetrable barrier to ultrarelativistic electrons in the Van Allen radiation belts, *Nature*, *515*(7528), 531–534, doi:10.1038/nature13956.

Blake, J. B., et al. (1995), CEPPAD: Comprehensive energetic particle and pitch angle distribution experiment on polar, *Space Sci. Rev.*, *71*, 531–562.

Blake, J. B., et al. (2013), The magnetic electron ion spectrometer (MagEIS) instruments aboard the Radiation Belt Storm Probes (RBSP) spacecraft, *Space Sci. Rev.*, doi:10.1007/s11214-013-9991-8.

Boyd, A. J., H. E. Spence, S. G. Claudepierre, J. F. Fennell, J. B. Blake, D. N. Baker, G. D. Reeves, and D. L. Turner (2014), Quantifying the radiation belt seed population in the 17 March 2013 electron acceleration event, *Geophys. Res. Lett.*, *41*, 2275–2281, doi:10.1002/2014GL059626.

Chen, Y., G. D. Reeves, and R. H. W. Friedel (2007), The energization of relativistic electrons in the outer Van Allen radiation belt, *Nat. Phys.*, *3*, 614–617, doi:10.1038/Nphys655.

Claudepierre, S. G., et al. (2015), A background correction algorithm for Van Allen Probes MagEIS electron flux measurements, *J. Geophys. Res. Space Physics*, *120*, 5703–5727, doi:10.1002/2015JA021171.

Fennell, J. F., S. G. Claudepierre, J. B. Blake, T. P. O'Brien, J. H. Clemmons, D. N. Baker, H. E. Spence, and G. D. Reeves (2015), Van Allen Probes show that the inner radiation zone contains no MeV electrons: ECT/MagEIS data, *Geophys. Res. Lett.*, *42*, 1283–1289, doi:10.1002/2014GL062874.

Friedel, R. H. W., A. Korth, and G. Kremser (1996), Substorm onsets observed by CRRES: Determination of energetic particle source regions, *J. Geophys. Res.*, *101*, 13,137–13,154, doi:10.1029/96JA00399.

Funsten, H. O., et al. (2013), Helium, Oxygen, Proton, and Electron (HOPE) mass spectrometer for the Radiation Belt Storm Probes mission, *Space Sci. Rev.*, doi:10.1007/s11214-013-9968-7.

Goldstein, J., S. Kanekal, D. N. Baker, and B. R. Sandel (2005), Dynamic relationship between the outer radiation belt and the plasmapause during March–May 2001, *Geophys. Res. Lett.*, *32*, L15104, doi:10.1029/2005GL023431.

Green, J. C., and M. G. Kivelson (2004), Relativistic electrons in the outer radiation belt: Differentiating between acceleration mechanisms, *J. Geophys. Res.*, *109*, A03213, doi:10.1029/2003JA010153.

Iles, R. H. A., N. P. Meredith, A. N. Fazakerley, and R. B. Horne (2006), Phase space density analysis of the outer radiation belt energetic electron dynamics, *J. Geophys. Res.*, *111*, A03204, doi:10.1029/2005JA011206.

Li, W., Q. Ma, R. M. Thorne, J. Bortnik, C. A. Kletzing, W. S. Kurth, G. B. Hospodarsky, and Y. Nishimura (2015), Statistical properties of plasmaspheric hiss derived from Van Allen Probes data and their effects on radiation belt electron dynamics, *J. Geophys. Res. Space Physics*, *120*, 3393–3405, doi:10.1002/2015JA021048.

Li, X., D. N. Baker, T. P. O'Brien, L. Xie, and Q. G. Zong (2006), Correlation between the inner edge of outer radiation belt electrons and the innermost plasmapause location, *Geophys. Res. Lett.*, *33*, L14107, doi:10.1029/2006GL026294.

Lyons, L. R., and R. M. Thorne (1973), Equilibrium structure of radiation belt electrons, *J. Geophys. Res.*, *78*, 2142–2149, doi:10.1029/JA078i013p02142.

Lyons, L. R., R. M. Thorne, and C. F. Kennel (1972), Pitch angle diffusion of radiation belt electrons within the plasmasphere, *J. Geophys. Res.*, *77*, 3455–3474, doi:10.1029/JA077i019p03455.

Malaspina, D. M., L. Andersson, R. E. Ergun, J. R. Wygant, J. W. Bonnell, C. Kletzing, G. D. Reeves, R. M. Skoug, and B. A. Larsen (2014), Nonlinear electric field structures in the inner magnetosphere, *Geophys. Res. Lett.*, *41*, 5693–5701, doi:10.1002/2014GL061109.

Mauk, B. H., N. J. Fox, S. G. Kanekal, R. L. Kessel, D. G. Sibeck, and A. Ukhorskiy (2012), Science objectives and rationale for the Radiation Belt Storm Probes mission, *Space Sci. Rev.*, doi:10.1007/s11214-012-9908-y.

Meredith, N. P., R. B. Horne, S. A. Glauert, R. M. Thorne, D. Summers, J. M. Albert, and R. R. Anderson (2006), Energetic outer zone electron loss timescales during low geomagnetic activity, *J. Geophys. Res.*, *111*, A05212, doi:10.1029/2005JA011516.

Meredith, N. P., R. B. Horne, S. A. Glauert, and R. R. Anderson (2007), Slot region electron loss timescales due to plasmaspheric hiss and lightning-generated whistlers, *J. Geophys. Res.*, *112*, A08214, doi:10.1029/2007JA012413.

Obara, T., T. Nagatsuma, M. Den, Y. Miyoshi, and A. Morioka (2000), Main-phase creation of 'seed' electrons in the outer radiation belt, *Earth Planets Space*, *52*, 41–47.

Pfitzer, K., S. Kane, and J. R. Winckler (1966), The spectra and intensity of electrons in the radiation belts, *Space Res.*, *6*, 702.

Reeves, G. D. (2015), Radiation belt electron acceleration and role of magnetotail, in *Magnetotails in the Solar System*, edited by A. Keiling, C. Jackman, and P. Delamere, pp. 345–359, John Wiley, Hoboken, N. J.

Reeves, G. D., M. G. Henderson, P. S. McLachlan, R. D. Belian, R. H. W. Friedel, and A. Korth (1996), Radial propagation of substorm injections, paper presented at 3rd International Conference on Substorms, ICS-3.

Reeves, G. D., K. L. McAdams, R. H. W. Friedel, and T. P. O'Brien (2003), Acceleration and loss of relativistic electrons during geomagnetic storms, *Geophys. Res. Lett.*, *30*(10), 1529, doi:10.1029/2002GL016513.

Reeves, G. D., et al. (2013), Electron acceleration in the heart of the Van Allen radiation belts, *Science*, *341*(6149), 991–994, doi:10.1126/science.1237743.

Reeves, G. D., A. Chan, and C. Rodger (2009), New directions for radiation belt research, *Space Weather*, *7*, doi:10.1029/2008SW000436.

Ripoll, J. F., J. M. Albert, and G. S. Cunningham (2014), Electron lifetimes from narrowband wave-particle interactions within the plasmasphere, *J. Geophys. Res. Space Physics*, *119*, 8858–8880, doi:10.1002/2014JA020217.

Ripoll, J. F., Y. Chen, J. F. Fennell, and R. H. W. Friedel (2015), On long decays of electrons in the vicinity of the slot region observed by HEO3, *J. Geophys. Res. Space Physics*, *120*, 460–478, doi:10.1002/2014JA020449.

Santolík, O., M. Parrot, L. R. O. Storey, J. S. Pickett, and D. A. Gurnett (2001), Propagation analysis of plasmaspheric hiss using polar pwi measurements, *Geophys. Res. Lett.*, *28*, 1127–1130, doi:10.1029/2000GL012239.

Spence, H. E., et al. (2013), Science goals and overview of the Energetic Particle, Composition, and Thermal Plasma (ECT) suite on NASA's Radiation Belt Storm Probes (RBSP) mission, *Space Sci. Rev.*, doi:10.1007/s11214-013-0007-5.

Summers, D., R. M. Thorne, and F. Xiao (1998), Relativistic theory of wave-particle resonant diffusion with application to electron acceleration in the magnetosphere, *J. Geophys. Res.*, *103*, 20,487–20,500, doi:10.1029/98JA01740.

Summers, D., B. Ni, and N. P. Meredith (2007), Timescales for radiation belt electron acceleration and loss due to resonant wave-particle interactions: 2. Evaluation for VLF chorus, ELF hiss, *J. Geophys. Res.*, *112*, A04207, doi:10.1029/2006JA011993.

Thaller, S. A., et al. (2015), Van Allen Probes investigation of the large-scale duskward electric field and its role in ring current formation and plasmasphere erosion in the 1 June 2013 storm, *J. Geophys. Res. Space Physics*, *120*, 4531–4543, doi:10.1002/2014JA020875.

Thorne, R. M., et al. (2013), Rapid local acceleration of relativistic radiation-belt electrons by magnetospheric chorus, *Nature*, *504*(7480), 411–414, doi:10.1038/nature12889.

Tu, W., G. S. Cunningham, Y. Chen, S. K. Morley, G. D. Reeves, J. B. Blake, D. N. Baker, and H. Spence (2014), Event-specific chorus wave and electron seed population models in DREAM3D using the Van Allen Probes, *Geophys. Res. Lett.*, *41*, 1359–1366, doi:10.1002/2013GL058819.

Turner, D. L., et al. (2015), Energetic electron injections deep into the inner magnetosphere associated with substorm activity, *Geophys. Res. Lett.*, *42*, 2079–2087, doi:10.1002/2015GL063225.

Vampola, A. L., J. V. Osborn, and B. M. Johnson (1992), CRRES magnetic electron spectrometer AFGL-701-5A (MEA), *J. Spacecr. Rockets*, *29*, 592–595.

Van Allen, J. A. (1959), The geomagnetically trapped corpuscular radiation, *J. Geophys. Res.*, *64*, 1683–1689, doi:10.1029/JZ064i011p01683.

Van Allen, J. A., and L. A. Frank (1959), Radiation around the Earth to a radial distance of 107,400 km, *Nature*, *183*, 430–434, doi:10.1038/183430a0.